

# SUPPLEMENTAL MATERIAL FOR: Geodynamic controls on slab window volcanism: Insights from the spatiotemporal evolution of the Coast Range Volcanics, California, USA

**Eliel S. C. Anttila<sup>1\*</sup>, John M. Cottle<sup>2</sup>, Demian A. Nelson<sup>2</sup>, Ryan P. Eden<sup>2</sup>, and Andrew Kylander-Clark<sup>2</sup>**

<sup>1</sup>*Department of Earth Sciences, ETH Zürich, Zürich, 8092, Switzerland*

<sup>2</sup>*Department of Earth Science, University of California Santa Barbara, Santa Barbara, CA, 93117, USA*

*\*Corresponding author: eanttila@ethz.ch*

## SUMMARY

This document contains descriptions of methods for all geochronological and geochemical analyses, data reduction protocols, a description of the integration of our geochronological and geochemical data into a paleogeographic model, two supplementary figures, and tables summarizing sample locations (Table S1), U-Pb zircon geochronological data (Table S2), zircon Hf isotope data (Table S3), and a compilation of legacy geochronology of the Coast Range Volcanics (Table S4). All supplemental material, data, and code for this work is accessible within the following GitHub repository:

[https://github.com/eliel-anttila/Anttila\\_et\\_al\\_Coast\\_Range\\_2025](https://github.com/eliel-anttila/Anttila_et_al_Coast_Range_2025)

## METHODS

### *Sample preparation*

Whole rock samples of broadly felsic (likely zircon-bearing) lithologies from Coast Range Volcanics localities (collected between 2011 and 2024; summarized in Table S1) were crushed in an industrial jaw crusher, and sieved to collect the resultant <500 micron grainsize fraction. This fraction was handwashed in an antiflocculant solution remove ultrafine material, and then hand-panned to isolate a heavy mineral fraction. Samples with heavy mineral fractions containing few zircon crystals were magnetically separated with a Franz device (0.4A at a 20° incline), and further separated by density in methylene iodide (MEI) to yield heavy-mineral separates. In addition to zircons processed and procured from to whole-rock samples, zircon separates for samples MT24 and OR24 (MT24-1 and OR24-2 of Gerasimov et al. [2024]) and IR22 and BM (IR22-1 and BM22-1 of Henschel et al. [2024]) were shared by N. Swanson-Hysell. Zircon crystals were individually picked from their respective mineral separates, mounted in epoxy, and polished. The internal structures of the zircons were mapped with cathodoluminescence (CL) imaging using a Cameca SX-100 Electron Probe Micro- Analyzer (EPMA) with a CL detector at UC Santa Barbara.

### *U-Pb zircon geochronology*

Laser ablation multi-collector inductively coupled plasma mass spectrometry (LA-ICP-MS) U-Pb geochronological analyses on zircon were completed at UC Santa Barbara, using a Cetac/Photon Machines Analyte Excite 193 nm excimer laser coupled with a Nu Plasma 3D multicollector ICP-MS, following the methods of Kylander-Clark et al. (2013). Each mounted

zircon was ablated with a 20 $\mu$ m laser spot. The zircon 91500 (Wiedenbeck et al., 1995) was used for age calibration. Secondary zircon reference materials included 9435, *AUSZ*, *Mudtank*, *GJI*, and *Plesovice* (Jackson et al., 2004). *Iolite* (Paton et al., 2010) was used to correct for U-Pb mass bias and drift following the methods of Kylander-Clark et al. (2013) and Horstwood et al. (2016). The resultant U and Pb isotopic ratios were reduced according to methods outlined in Kylander-Clark et al. (2013). Dates for each analyzed grain were calculated by importing reduced U and Pb isotope ratios into *IsoplotR* (Vermeesch, 2018). Reduced ratios and all resultant dates are tabulated in Table S2.

For each sample, a group of zircons with young  $^{206}\text{Pb}/^{238}\text{U}$  dates were identified. These analyses were used to calculate a weighted-mean age: the oldest analyses were iteratively removed until a group of zircon ages conforming to statistical standards for a single population (Wendt and Carl, 1991) was acquired. The data used to calculate these weighted mean ages are in non-italicized text in Table S2; analyses that did not go into the weighted mean (likely representing magmatic inheritance) are italicized. A blanket systematic uncertainty of 2%, accounting for all uncertainty criteria outlined in Horstwood et al. (2016), was then applied to the calculated weighted-mean ages for each sample. Weighted-mean ages for each sample are tabulated in Table S1.

#### *U-Pb ages of the Coast Range Volcanics*

Zircon U-Pb weighted-mean ages from CRV centers are broadly older than extant K-Ar system ages for the same localities (Stanley et al., 2000; Fig. 1, main manuscript), and offer better analytical precision and reproducibility (Fig. S1). Relatively-older zircon U-Pb ages may result from the higher closure temperature of the zircon U-Pb system ( $\sim 950^\circ\text{C}$ , Cherniak and Watson, 2001) relative to  $^{39}\text{Ar}/^{40}\text{Ar}$  closure temperatures (between  $\sim 220^\circ\text{C}$  [in orthoclase; Foland, 1994] and  $\sim 540^\circ\text{C}$  [in Mg-hornblende; Harrison, 1982]). A statistically-homogenous (sensu Wendt and Carl, 1991) population of young zircon is present in each sample, likely reflecting similar crystallization processes occurring at each locality and allowing the direct comparison of all U-Pb ages in this study.

#### *Zircon Hf Isotopes*

Zircon crystals that were integrated into the weighted-mean ages calculated for each sample (e.g. those with young  $^{206}\text{Pb}/^{238}\text{U}$  dates) were identified and subsequently targeted for zircon Hf isotope measurements. Zircon Hf isotopes were measured via LA-MC-ICP-MS at UC Santa Barbara, using the same Cetac/Photon Machines Analyte Excite 193 nm excimer laser coupled with a Nu Plasma 3D MC-ICP-MS used to develop U-Pb data. Laser shots, with a diameter of 40 $\mu$ m, were set coaxially with the 20 $\mu$ m pits from prior U-Pb analyses, such that the Hf isotope measurement ablation pits overlap with the U-Pb pits; note that for smaller crystals, Hf isotope shots were occasionally placed off-axis from extant U-Pb pits to maximize overlap with the zircon crystal itself. Zircons with a b-axis width of less than 40 $\mu$ m were excluded from the Hf isotope measurement campaign. Laser energy was 4mJ, at a repetition rate of 8 hz over 60-second ablation periods with a 30-second washout interval. The zircon *Plešovice* ( $^{176}\text{Hf}/^{177}\text{Hf} = 0.282482 \pm 13\text{E-}06$ ; Sláma et al., 2008) was measured as a reference material throughout all analytical runs; *GJI* ( $^{176}\text{Hf}/^{177}\text{Hf} = 0.282000 \pm 5\text{E-}06$ ; Morel et al., 2008), *MUN-1* ( $0.282135 \pm 7\text{E-}06$ ; Fisher et al., 2011) and *MudTank* ( $0.282523 \pm 5.9\text{E-}05$ ; Gain et al., 2019) served as secondary reference materials. Zircon Hf data was corrected for mass bias and reduced in *Iolite* (Paton et al., 2011). Individual analyses with unstable peak behavior (characterized by rapid or

unstable variations in isotopic ratio or peak intensity during a measurement) were identified, screened, and removed during data reduction in Iolite. Across all analytical runs, corrected  $^{176}\text{Hf}/^{177}\text{Hf}$  ratios of the *Plešovice* reference material yielded a mean of 0.282486.

$\epsilon\text{Hf}_i$  values were calculated for each measured zircon relative to the chondritic uniform reservoir (CHUR; present-day  $^{176}\text{Hf}/^{177}\text{Hf} = 0.282772$  and  $^{176}\text{Lu}/^{177}\text{Hf} = 0.0332$ ; Vervoort and Blichert-Toft, 1999) using the corresponding single-grain  $^{206}\text{Pb}/^{238}\text{U}$  age of the measured zircon, and a  $^{176}\text{Lu}$  decay constant of  $1.867 \times 10^{-11} \text{ yr}^{-1}$  (Söderlund et al., 2004). All reduced zircon  $^{176}\text{Hf}/^{177}\text{Hf}$  and  $^{176}\text{Lu}/^{177}\text{Hf}$  ratios, as well as corresponding  $^{206}\text{Pb}/^{238}\text{U}$  ages and  $\epsilon\text{Hf}_i$  values for all CRV zircon, are reported in Table S3. Individual analyses with  $\epsilon\text{Hf}_i$  greater than that of depleted mantle (Vervoort, 2014) may be the result of high Yb content, or could potentially represent the melting or incorporation of an enigmatic, highly Hf-depleted source. As such, analyses with  $\epsilon\text{Hf}_i$  greater than that of depleted mantle are not included in calculations of mean  $\epsilon\text{Hf}_i$  for each CRV locality, are presented as light gray points on Fig. 2 of the main text, and are italicized in Table S3.

## IMPLEMENTATION OF PALEO GEOGRAPHIC RECONSTRUCTION MODEL

All CRV ages and modern locations were integrated into the paleogeographic reconstruction model of Wilson et al. (2005), which utilizes a diverse array of geological datasets and constraints to build a fault-block-based reconstruction of the development of the Pacific-North American transform margin over the past ca. 30 Myr. Model block motions and rotations have been adapted into a GPlates (<https://www.gplates.org/>)-compatible format; .rot and block geometry files (courtesy of D. Wilson, personal communication, 2021) used to run the model in gPlates are available in the following repository: [https://github.com/eliel-anttila/Anttila\\_et\\_al\\_Coast\\_Range\\_2025/tree/main/Reconstruction\\_and\\_Mapping](https://github.com/eliel-anttila/Anttila_et_al_Coast_Range_2025/tree/main/Reconstruction_and_Mapping). Each CRV locality was associated with a specific block in the reconstruction model (Table S1), typically by linking the CRV site with the block that is spatially-correlative with the modern location of the CRV locality. The syn-emplacement paleogeographic location of each CRV locality was modeled by calculating the position of each locality at the reconstruction model time equivalent to the age of the eruptive center.

There are two necessary exceptions to this workflow, both indicated with an asterisk in the *PlateID* column of Table S1. The first concerns the paleogeographic reconstruction of sample IR22 (Northbrae Volcanics; sample IR22-1 of Henschel et al., 2024), the present location of which is within the extent of Plate 10 in the reconstruction framework (Wilson et al., 2005). Plate 10 includes a portion of the San Francisco Bay Area found west of the Hayward Fault, but east of the San Andreas Fault; this entire region is treated as a single block throughout the duration of the reconstruction model of Wilson et al. (2005). However, the Northbrae Volcanics (IR22) have been correlated with the Burdell Mountain Volcanics (BM), implying dextral offset within Plate 10 of ca. 40 km. Furthermore, it remains unclear whether the paleo-Hayward fault was located west or east of the current location of the Northbrae Volcanics, introducing uncertainty into the magnitude of offset of IR22 relative to the total displacement of Plate 10. We adopt the paleogeographically-restored location of the Burdell Mountain Volcanics, tied to the motion of Plate 10, ca. 11 Ma as the emplacement location of both BM22 and IR22; IR22 is the only locality to be manually moved (to spatiotemporally correlate with the restored location of BM22) in the reconstruction.

The second exception revolves around the WR1 locality (Wagon Road Canyon volcanics, Vedder et al., 1973), which is presently located on Plate 32 in the Wilson et al. (2005) model,

just west of the “Big Bend” in the San Andreas Fault (e.g. Crowell, 1979). In the Wilson et al. (2005) model, Plate 32 is dextrally offset west of a proto-San Andreas transform fault throughout the progression of the model. However, the timing of the generation/incorporation of the Big Bend into the proto-San Andreas fault remains uncertain, as is the timing of the incipience of dextral offset along faults east of Plate 32 (e.g. the present-day San Andreas fault trace). As such, we present two end-member models for the restored emplacement location of WR1. WR1a (Fig. 3, main manuscript), tied to Plate 35 (located east of the modern San Andreas Fault), minimizes dextral offset of Plate 32 along the proto-San Andreas. The reconstructed location WR1b (Fig. 3, main manuscript) shows the full potential displacement of WR1 tied to Plate 32 given dextral offset along a long-lived proto-San Andreas fault located east of Plate 32. We posit that the correct reconstructed location of WR1 lies somewhere between these two end-member locations.

Shapefiles of all localities with new U-Pb ages, and their reconstructed locations, are available in the project repository ([https://github.com/eliel-anttila/Anttila\\_et\\_al\\_Coast\\_Range\\_2025/tree/main/Reconstruction\\_and\\_Mapping/Shapefiles](https://github.com/eliel-anttila/Anttila_et_al_Coast_Range_2025/tree/main/Reconstruction_and_Mapping/Shapefiles)).

## REFERENCES

- Atwater, T., & Stock, J. (1998). Pacific-North America plate tectonics of the Neogene southwestern United States: an update. *International Geology Review*, 40(5), 375-402.
- Balbas, A., Konrad, K., Onderdonk, N., Castillo, P. R., & Behl, R. (2024). Oligocene and Miocene blowtorch volcanism within the California Borderland and its influence on the plate-boundary transition. *Geology*, 52(8), 600-604.
- Cherniak, D. J., & Watson, E. B. (2001). Pb diffusion in zircon. *Chemical Geology*, 172(1-2), 5-24. [https://doi.org/10.1016/S0009-2541\(00\)00233-3](https://doi.org/10.1016/S0009-2541(00)00233-3)
- Coleman, R. G., Gooley, J. T., Gregory, R. T., & Graham, S. A. (2022). New Idria serpentinite protrusion, Diablo Range, California: From upper mantle to the surface. *American Journal of Science*, 322(4), 533-560.
- Crowell, J. C. (1979). The San Andreas fault system through time. *Journal of the Geological Society*, 136(3), 293-302.
- Fisher, C. M., Hanchar, J. M., Samson, S. D., Dhuime, B., Blichert-Toft, J., Vervoort, J. D., & Lam, R. (2011). Synthetic zircon doped with hafnium and rare earth elements: A reference material for in situ hafnium isotope analysis. *Chemical Geology*, 286(1-2), 32-47.
- Foland, K. A. (1994). Argon diffusion in feldspars. In *Feldspars and their reactions* (pp. 415-447). Dordrecht: Springer Netherlands.
- Gain, S. E., Gréau, Y., Henry, H., Belousova, E., Dainis, I., Griffin, W. L., & O'reilly, S. Y. (2019). Mud Tank Zircon: Long-term evaluation of a reference material for U-Pb dating, Hf-isotope analysis and trace element analysis. *Geostandards and Geoanalytical Research*, 43(3), 339-354.
- Gerasimov, S. H., Hodgins, E. B., Crowley, J. L., & Swanson-Hysell, N. L. (2024). Chronostratigraphy of Miocene strata in the Berkeley Hills (California Coast Ranges, USA) and the arrival of the San Andreas transform boundary. *Geosphere*, 20(1), 162-178.
- Harrison, Mark T. (1982). Diffusion of <sup>40</sup>Ar in hornblende. *Contributions to Mineralogy and Petrology*, 78, 324-331.

- Henschel, W. G., Hodgins, E. B., Grimsich, J. L., & Swanson-Hysell, N. L. (2024). The Northbrae rhyolite of Berkeley (California, USA) constrains motion of the proto-Hayward Fault. *International Geology Review*, 1-15.
- Horstwood, M. S., Košler, J., Gehrels, G., Jackson, S. E., McLean, N. M., Paton, C., ... & Schoene, B. (2016). Community-derived standards for LA-ICP-MS U-(Th) Pb geochronology—Uncertainty propagation, age interpretation and data reporting. *Geostandards and Geoanalytical Research*, 40(3), 311-332.
- Jackson, S. E., Pearson, N. J., Griffin, W. L., & Belousova, E. A. (2004). The application of laser ablation-inductively coupled plasma-mass spectrometry to in situ U–Pb zircon geochronology. *Chemical geology*, 211(1-2), 47-69.
- Kylander-Clark, A. R., Hacker, B. R., & Cottle, J. M. (2013). Laser-ablation split-stream ICP petrochronology. *Chemical Geology*, 345, 99-112.
- Morel, M. L. A., Nebel, O., Nebel-Jacobsen, Y. J., Miller, J. S., & Vroon, P. Z. (2008). Hafnium isotope characterization of the GJ-1 zircon reference material by solution and laser-ablation MC-ICPMS. *Chemical geology*, 255(1-2), 231-235.
- Pampeyan, Earl H. *Geologic map of the Palo Alto and part of the Redwood Point 7-1/2' quadrangles, San Mateo and Santa Clara Counties, California*. No. 2371. US Geological Survey, 1993.
- Paton, C., Hellstrom, J., Paul, B., Woodhead, J., & Hergt, J. (2011). Iolite: Freeware for the visualisation and processing of mass spectrometric data. *Journal of Analytical Atomic Spectrometry*, 26(12), 2508-2518.
- Sláma, J., Košler, J., Condon, D. J., Crowley, J. L., Gerdes, A., Hanchar, J. M., ... & Whitehouse, M. J. (2008). Plešovice zircon—a new natural reference material for U–Pb and Hf isotopic microanalysis. *Chemical geology*, 249(1-2), 1-35.
- Söderlund, U., Patchett, P. J., Vervoort, J. D., & Isachsen, C. E. (2004). The  $^{176}\text{Lu}$  decay constant determined by Lu–Hf and U–Pb isotope systematics of Precambrian mafic intrusions. *Earth and Planetary Science Letters*, 219(3-4), 311-324.
- Stanley, R. G. (1987). Implications of the northwestwardly younger age of the volcanic rocks of west-central California: Alternative interpretation. *GSA Bulletin*, 98(5), 612-614.
- Vedder, J.G., Dibblee, T.W., Jr., and Brown, R.D., 1973, Geologic map of the upper Mono Creek–Pine Mountain area, California: U.S. Geological Survey Miscellaneous Geologic Investigations Map I–752, scale 1:48,000.
- Vermeesch, P. (2018). IsoplotR: A free and open toolbox for geochronology. *Geoscience Frontiers*, 9(5), 1479-1493.
- Vervoort, J. (2014). Lu–Hf Dating: The Lu–Hf Isotope System. In: Rink, W., Thompson, J. (eds). *Encyclopedia of Scientific Dating Methods*. Springer, Dordrecht. [https://doi.org/10.1007/978-94-007-6326-5\\_46-1](https://doi.org/10.1007/978-94-007-6326-5_46-1)
- Vervoort, J. D., & Blichert-Toft, J. (1999). Evolution of the depleted mantle: Hf isotope evidence from juvenile rocks through time. *Geochimica et cosmochimica acta*, 63(3-4), 533-556.
- Wendt, I., & Carl, C. (1991). The statistical distribution of the mean squared weighted deviation. *Chemical Geology: Isotope Geoscience Section*, 86(4), 275-285.
- Wakabayashi, J. (1999). Distribution of displacement on and evolution of a young transform fault system: the northern San Andreas fault system, California. *Tectonics*, 18(6), 1245-1274.

Wiedenbeck, M. A. P. C., P. Alle, F. Y. Corfu, William L. Griffin, M. Meier, F. V. Oberli, A. von Quadt, J. C. Roddick, and W. Spiegel. "Three natural zircon standards for U-Th-Pb, Lu-Hf, trace element and REE analyses." *Geostandards newsletter* 19, no. 1 (1995): 1-23.

Wilson, D. S., McCrory, P. A., & Stanley, R. G. (2005). Implications of volcanism in coastal California for the Neogene deformation history of western North America. *Tectonics*, 24(3).

## SUPPLEMENTAL FIGURES

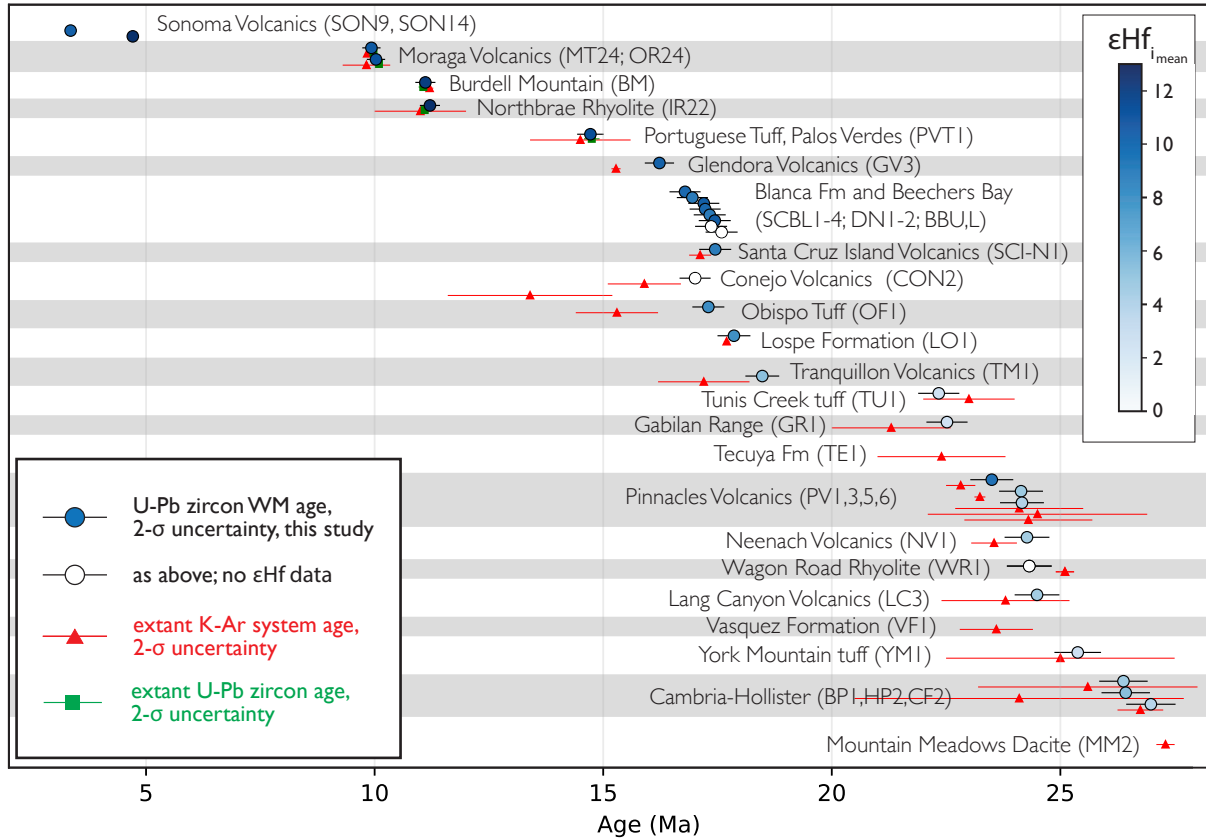


**Figure S1:** Age and 2 $\sigma$  uncertainty of all localities dated with U-Pb LA-MC-ICP-MS geochronology in this study, plotted with prior K-Ar system or U-Pb zircon ages for each locality. Data and references utilized in this figure can be found here: [https://github.com/eliel-anttila/Anttila\\_et\\_al\\_Coast\\_Range\\_2024/blob/main/Code/Data/CRV\\_Upb\\_summary.csv](https://github.com/eliel-anttila/Anttila_et_al_Coast_Range_2024/blob/main/Code/Data/CRV_Upb_summary.csv)

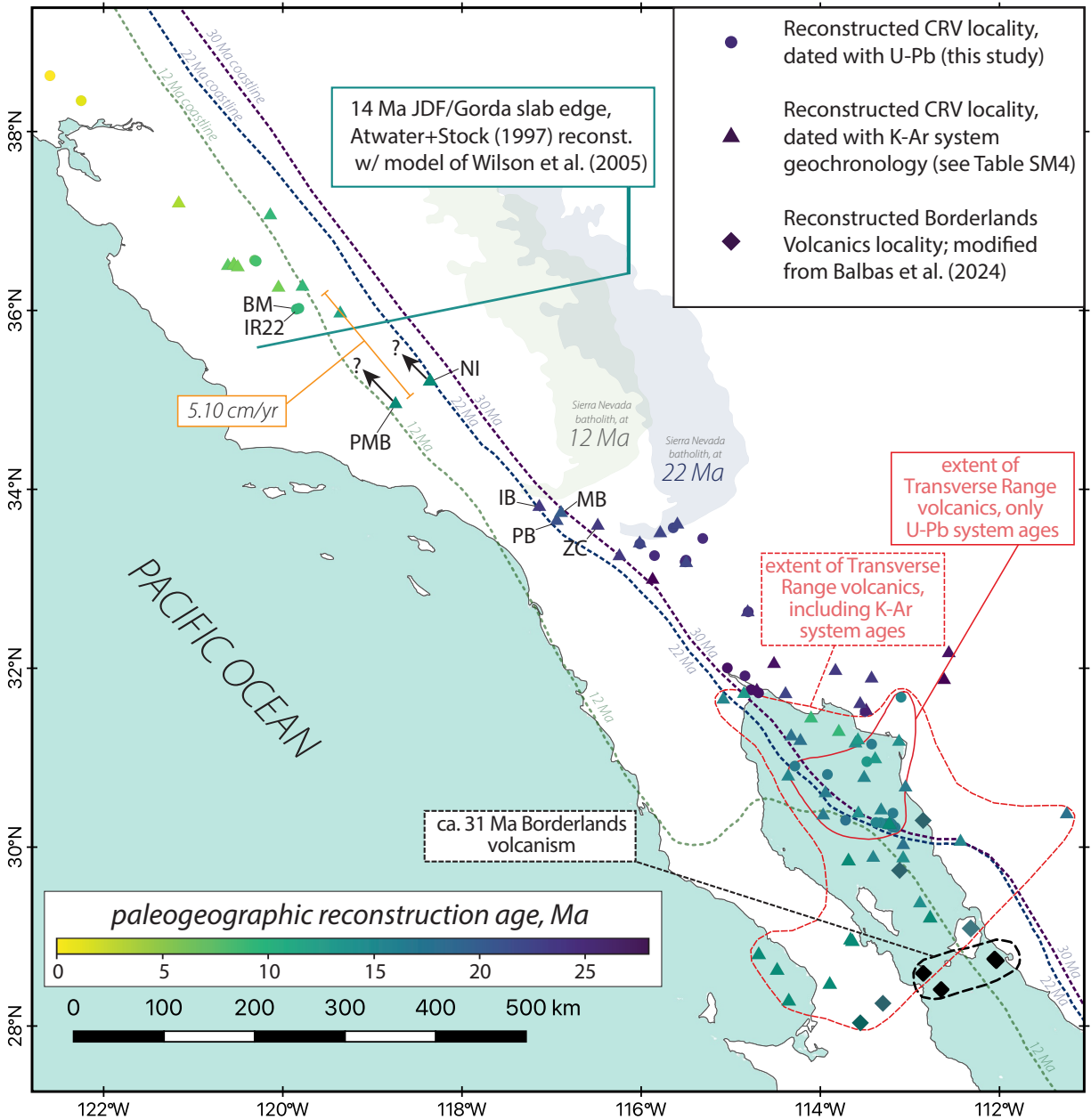


**Figure S2:** Paleogeographically reconstructed locations of CRV localities dated with U-Pb zircon geochronology (circles, this study), and K-Ar system geochronology (triangles, references in Table S4), as well as the syneruptive reconstructed locations of California Borderlands volcanics (diamonds, modern day locations and ages from Balbas et al., 2024, and references therein). A solid red outline denotes the extent of Transverse Ranges CRV localities constrained with U-Pb geochronology (sensu Fig. 3, main text), while the dashed red line encircles the reconstructed locations of ca. 15-18 Ma volcanism, including both Transverse Range-proximal CRV localities (see Table S4) and California Borderlands localities constrained by K-Ar system geochronology. A black dashed line encircles the reconstructed location of ca. 31 Ma volcanism in the distal Borderlands, interpreted to record an initial ridge-trench interaction along this portion of the margin (Balbas et al. 2024). Green, blue, and purple fine-dashed lines denote the approximate reconstructed North American coastline at 12 Ma, 22 Ma, and 30 Ma, respectively. Note the

apparent incursion of the reconstructed emplacement locations of the Page Mill Basalt (PMB), New Idria alkali basalt dikes (NI), Iversen Basalt (IB), Mindego Basalt (MB), Vaqueros intrusives (PB) and Zayante Creek intrusives (ZC) into the spatiotemporal gap in NW-trending volcanism observed in samples dated with U-Pb zircon geochronology. Analytical uncertainties on the K-Ar system ages of IB, MB, PB, and ZC all exceed 1.4 Ma ( $2\sigma$ ; Table S4), thus introducing significant uncertainty into the restored locations plotted in this figure. We emphasize that the incorporation of ages with large analytical uncertainties into a paleogeographic reconstruction greatly magnifies the uncertainty of the reconstructed emplacement locality. This is particularly applicable to the reconstructed locations of localities where reported radiometric analytical uncertainties do not capture broader uncertainties about emplacement/eruptive age (see discussion of the age of the Mindego Basalt in Stanley, 1987). Similarly, the Page Mill Basalt (PMB) locality has K-Ar system age control ranging from ca. 16 Ma (unpublished data of Swisher, 1999, reported in Wakabayashi, 1999) to ca. 12 Ma (Wakabayashi, 1999), with other data (both published and unpublished, reported in Pampeyan, 1993) supporting an age of ca. 14 Ma (14 Ma reconstructed location shown here). Analytical uncertainties of reported PMB ages allow an emplacement/eruptive age of ca. 12 Ma, which would move the restored location of the PMB to the north and minimize the apparent overlap of the PMB with the 22-12 Ma gap in NW-trending CRV activity observed in localities dated with U-Pb geochronology. Uncertainties on the age of the New Idria (NI) alkali basalt dikes (Coleman et al., 2022) allow for a similar northward shift of the paleogeographically reconstructed eruptive location of this locality. However, we note that the rate of NW-younging migration of CRV volcanism between the ca. 14 Ma reconstructed localities of PMB/NI and the ca. 11 Ma reconstructed localities (BM/IR22) is approximately 5.10 cm/yr, comparable to other rates calculated along well-constrained segments of the NW-younging trend (Fig. 3, main text). Thus, the 14 Ma reconstructed locations of PMB and NI may serve as a reasonable spatiotemporal southern end-member for the resumption of NW-younging CRV volcanism following the gap in the NW-younging trend.